Acta Materialia 105 (2016) 258–272

Contents lists available at ScienceDirect

Acta Materialia

journal homepage: www.elsevier.com/locate/actamat

Full length article

Structural characterization of ultrafine-grained interstitial-free steel prepared by severe plastic deformation

J. Čížek [a,*], M. Janeček [b], T. Krajňák [b], J. Stráská [b], P. Hruška [a], J. Gubicza [c], H.S. Kim [d]

[a] Faculty of Mathematics and Physics, Charles University in Prague, Department of Low Temperature Physics, V Holešovičkách 2, Prague 8, CZ-18000, Czech Republic
[b] Faculty of Mathematics and Physics, Charles University in Prague, Department of Physics of Materials, Ke Karlovu 5, Prague 2, CZ-12116, Czech Republic
[c] Department of Materials Physics, Eötvös Loránd University, Budapest, P.O.B. 32, H-1518, Hungary
[d] Department of Materials Science and Engineering, POSTECH, Pohang 790-784, South Korea

ARTICLE INFO

Article history:
Received 2 June 2015
Received in revised form
11 November 2015
Accepted 23 December 2015
Available online xxx

Keywords:
Interstitial free steel
Ultrafine-grained materials
Severe plastic deformation
Positron annihilation
X-ray diffraction

ABSTRACT

Interstitial free steel with ultrafine-grained (UFG) structure was prepared by high-pressure torsion (HPT). The development of the microstructure as a function of the number of HPT turns was studied at the centre, half-radius and periphery of the HPT-processed disks by X-ray line profile analysis (XLPA), positron annihilation spectroscopy (PAS) and electron microscopy. The dislocation densities and the dislocation cell sizes determined by XLPA were found to be in good agreement with those obtained by PAS. The evolution of the dislocation density, the dislocation cell and grain sizes, the vacancy cluster size, as well as the high-angle grain boundary (HAGB) fraction was determined as a function of the equivalent strain. It was found that first the dislocation density saturated, then the dislocation cell size reached its minimum value and finally the grain size got saturated. For very high strains after the saturation of grain size the HAGB fraction further increased. The PAS investigations revealed that vacancies introduced by severe plastic deformation agglomerated into small clusters consisting of 9–14 vacancies. The evolution of the yield strength calculated from the microhardness as a function of strain was explained by the development of the defect structure.

© 2015 Acta Materialia Inc. Published by Elsevier Ltd. All rights reserved.

1. Introduction

Severe plastic deformation (SPD) is an attractive method which enables to achieve extremely strong grain refinement [1]. Bulk ultrafine-grained (UFG) materials with grain size in the range 100–500 nm can be produced by advanced techniques based on repeated application of SPD [2]. Because of high density of grain boundaries UFG materials often exhibit high strength while retaining appreciable level of ductility [3]. Among a variety of SPD-based techniques developed so far high-pressure torsion (HPT) is the most efficient in grain refinement [2,4]. In HPT processing a disk shaped sample located between two anvils is subjected to compressive pressure of several GPa and simultaneously strained by a repeated rotating of one anvil allowing to impose high strain to the material. In order to fully understand grain refinement by SPD it is important to examine the development of microstructure during HPT processing.

The strain imposed to the sample during HPT processing is not uniform but increases from the centre of the sample (corresponding to the rotation axis) towards the periphery [2,4,5]. The equivalent strain of a sample subjected to N HPT revolutions can be estimated from the relation [2].

$$e_{equiv} = \frac{1}{\sqrt{3}} \frac{2\pi rN}{h}, \tag{1}$$

where h is the thickness of the deformed sample and r is the radial distance from the centre, see Fig. 1a. Owing to the non-uniform strain, the homogeneity of UFG structure across the HPT-deformed sample is a very important issue which has been extensively studied in the recent years [6–10].

Interstitial-free (IF) steels constitute an important class of steels having carbon content less than 0.01 wt%. These steels are widely used in automobile industry as sheet material due to their excellent deep drawability as a result of the low content of interstitial solutes and a particular texture in cold rolled state [11–13]. In the recent

* Corresponding author.
E-mail address: jakub.cizek@mff.cuni.cz (J. Čížek).

http://dx.doi.org/10.1016/j.actamat.2015.12.039
1359-6454/© 2015 Acta Materialia Inc. Published by Elsevier Ltd. All rights reserved.

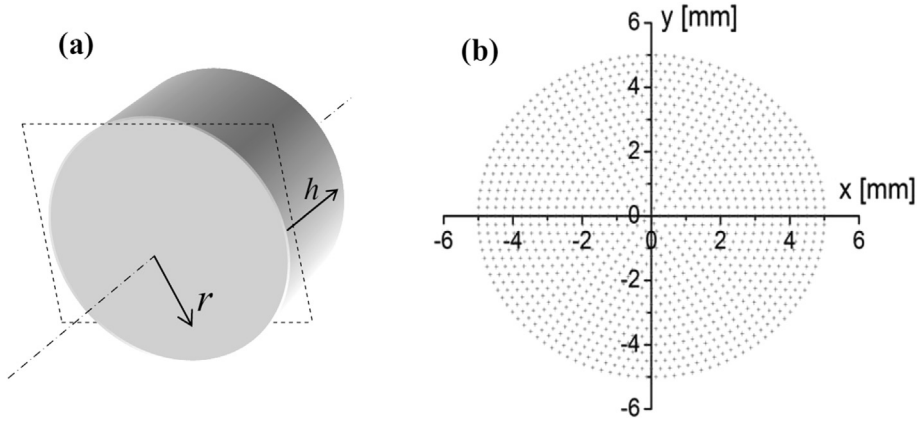

Fig. 1. (a) Schematic illustration of HPT-deformed specimen with thickness *h*. The radial distance from the centre is denoted by the symbol *r*. (b) Mesh used for microhardness mapping.

years, efforts have been made to improve the strength of this class of steels by means of grain refinement through SPD procedures [14,15].

The objective of this work was the investigation of microstructure development in IF steel during HPT processing. Lattice defects play a very important role in the determination of the properties of UFG materials since SPD introduces a high density of dislocations [2,14,15] and also a large concentration of vacancies [16–19]. This requires employment of techniques capable of quantitative characterization of lattice defects in UFG materials.

The X-ray line-profile analysis (XLPA) [20] allows determining the mean crystallite size and the lattice strain. Since in UFG materials prepared by SPD the lattice distortions are primarily caused by dislocations, the mean dislocation density can be obtained by XLPA. The XLPA technique has been frequently employed for characterization of UFG structure in a variety of materials [14,15,21,22]. In particular, the Convolutional Multiple Whole Profile (CMWP) fitting method [20,23] become very popular for the analysis of X-ray diffraction patterns and determination of the crystallite size and the mean dislocation density.

The positron annihilation spectroscopy (PAS) [24] is a well-developed non-destructive technique with a high sensitivity to open-volume defects, e.g. vacancies, dislocations and vacancy clusters, and has been successfully utilized for defects studies of UFG materials [18,19,25–27]. The PAS studies revealed that in addition to dislocations SPD introduces also a high concentration of vacancies which agglomerate into small vacancy clusters [19,28]. The concentration of defects can be calculated from PAS parameters using a suitable trapping model. So called simple trapping model (STM) [29] is usually employed for the analysis of PAS data. However, STM is based on the assumption that defects are distributed uniformly, i.e. positron trapping rates are constant in the whole sample. This is, however, often not the case for dislocations in UFG materials prepared by SPD since cellular dislocation structure is formed in metals with medium to high stacking fault energy (e.g. Fe, Cu and Al) subjected to plastic deformation [30–32]. Grains separated by geometrically necessary grain boundaries comprise of dislocation cells delineated by dislocation walls (incidental dislocation boundaries) [33,34]. In the cell interiors the dislocation density is low, while the dislocation walls exhibit very high density of dislocations [35,36]. Non-uniform spatial distribution of dislocations leads to spatially dependent positron trapping rate since the probability for positron trapping at dislocation walls is much higher than in the cell interiors. A so called diffusion trapping model (DTM) [26,37] was developed to describe properly the kinetic of positron trapping in UFG materials. The UFG sample is divided into spherical shape almost dislocation-free cells with a diameter *d* and dislocation walls containing very high density of dislocations. Positrons thermalized inside the dislocation walls are very quickly trapped at dislocations there. Positrons thermalized inside the cell interiors may reach dislocation walls by diffusion and be trapped there as well. This is taken into account in DTM by solution of the positron diffusion-annihilation equation [38]. Analysis of PAS data in the frame of DTM enables to determine important microstructural features of the UFG material: the average size of dislocation cells *d*, the volume fraction η of dislocation walls, and the dislocation density in the dislocation walls $\rho_{D,\mathrm{wall}}$. The mean dislocation density can be then obtained as

$$\rho_D = \rho_{D,\mathrm{wall}}\ \eta.$$

The DTM has been successfully applied for microstructure investigations of UFG Cu prepared by HPT [26], UFG Al [27] processed by equal channel angular pressing and also for characterization of sub-surface damage in machined steels [39].

The size of dislocation cells determined by DTM is expected to be comparable to the mean crystallite size (mean size of coherently scattering domains) provided by XLPA. Hence, both XLPA and PAS are non-destructive techniques capable of determination of important structural parameters of UFG materials, namely the size of dislocation cells and the dislocation density. But a systematic study involving both XLPA and PAS is still missing in the literature. Such a study is highly desirable not only to verify the consistence of the models used by these two techniques but also to extend the range of accessible dislocation densities and cell dimensions using the combination of these two techniques. On one hand, PAS is more sensitive to dislocations and enables to determine the dislocation density even below the sensitivity threshold of XLPA. On the other hand, XLPA provides reliable estimation of dislocation density in samples containing very high number of dislocations which causes saturated trapping of positrons. A comparative XLPA and PAS study of the development of UFG structure in IF steels subjected to HPT processing was performed in the present work.

PAS and XLPA spectroscopic techniques were supported by direct observations of UFG structure by means of electron microscopy. Microhardness testing was employed to correlate the development of microstructure with variations of mechanical properties. Inhomogeneities of the microstructure of HPT-deformed specimens were mapped by microhardness and also by spatially resolved PAS. As it was demonstrated in Ref. [10] these

techniques are sensitive to different aspects of microstructure and provide complementary information about the development of UFG structure during HPT processing. While microhardness mapping is sensitive to dislocation density and grain size, PAS mapping reflects spatial distribution of dislocations and deformation-induced vacancies.

2. Experimental

2.1. Samples

IF steel with a composition of 0.0026 wt% C, 0.096 wt% Mn, 0.045 wt% Al, and 0.041 wt% Ti was provided by the Pohang Steel Company (POSCO), Korea. The as-received material was homogenized at 700 °C for 2 h and furnace cooled.

For HPT deformation, disks with the thickness of 1 mm and the radius of 5 mm were cut from the homogenized billet using a diamond saw. A series of specimens with different number of turns $N = 1/4, 1/2, 1, 3$ and 5 was processed by HPT at room temperature using the pressure of 2.5 GPa. Additionally, a specimen which was only pressed under the same pressure of 2.5 GPa but without torsion straining was also prepared. This sample is denoted $N = 0$.

2.2. Electron microscopy

Microstructure of steel samples was investigated by high resolution scanning electron microscope FEI Quanta 200 FEG operated at 10 kV using backscattered electrons. For final surface treatment polishing in a Colloidal silica solution, containing 40 nm particles, for 30 s was used. Employing channelling contrast revealed the grain structure. Electron back-scatter diffraction (EBSD) was used to investigate the details of microstructure evolution in HPT disk specimens. The area examined by EBSD was approximately 100×100 μm^2 and the step size was set as 100 nm. EBSD investigations were performed at the centre ($r = 0$), at the half radius ($r = 2.5$ mm) and at the periphery ($r = 4$ mm) of individual disk specimens.

2.3. Microhardness testing

Automatic microhardness tester Qness Q10a was utilized for Vickers microhardness (HV) mapping (the applied load of 500 g and the holding time of 10 s were used). Homogeneity of HPT-deformed samples was mapped using a regular network of indents consisting of concentric circles with the radius step of 0.25 mm and the tangential distance of 0.25 mm along each circle, see Fig. 1b. HV map on each specimen consisted of 1100 indents.

2.4. PAS

PAS investigations were performed using a $^{22}NaCO_3$ positron source with the activity of ≈1 MBq. The source spot was carefully deposited on a 2 μm thick mylar foil so that the spot diameter was smaller than 1 mm.

A digital spectrometer [40] with time resolution of 145 ps (FWHM of the resolution function) was employed for positron lifetime (LT) spectroscopy. At least 10^7 positron annihilation events were collected in each LT spectrum which was subsequently decomposed into exponential components by a maximum likelihood code [41]. A well annealed α-Fe reference sample characterized by a single component LT spectrum with lifetime of (107.5 ± 0.4) ps was used to determine the source contribution to the LT spectra. It consisted of two components with lifetimes (368 ± 1) ps and (1.5 ± 0.1) ns and corresponding relative intensities (9.5 ± 0.2) and (1.2 ± 0.2) %, respectively. These contributions come from positrons annihilated in the $^{22}NaCO_3$ source spot and the covering mylar foils and were always subtracted from the spectra.

Mapping of the lateral distribution of defects in the HPT-deformed samples was performed by means of spatially resolved Doppler-broadening (DB) spectroscopy [19]. Spatially resolved DB measurements were performed by positioning the positron source spot at various radial distances from the centre of the sample disk using an x-y moving stage. The uncertainty in position of the positron source was ≈0.1 mm. The DB of annihilation radiation was measured by a high purity germanium (HPGe) detector with energy resolution of 1.30 keV at 511 keV. At least 5×10^5 counts were accumulated in the annihilation peak in each spectrum. The DB of the annihilation peak was evaluated using the line shape S parameter. The central region for calculation of the S parameter was chosen symmetrically around the 511 keV annihilation peak from 510.07 to 511.93 keV. All S values presented in this work were normalized to the S parameter $S_0 = 0.5026(5)$ measured in the well annealed α-Fe reference specimen.

2.5. XLPA

The microstructure of the HPT-processed IF steel samples was studied by XLPA along the radius of the sample disks. The X-ray line profiles were measured by a high-resolution diffractometer with $CoK_{\alpha 1}$ radiation (wavelength: $\lambda = 0.1789$ nm). The line profiles were evaluated by CMWP fitting method [20,23]. In this procedure, the diffraction pattern is fitted by the sum of a background spline and the convolution of the instrumental pattern and the theoretical line profiles related to the crystallite size and dislocations. Because of the UFG microstructure of the studied samples, the physical broadening of the profiles was much larger than the instrumental broadening, therefore instrumental correction was not applied in the evaluation. The theoretical profile functions used in this fitting procedure are calculated on the basis of a model of the microstructure, where the crystallites have spherical shape and log-normal size distribution.

The following parameters of the microstructure were obtained from CMWP fitting procedure: the area-weighted mean crystallite size d, the mean dislocation density ρ_D, the parameter q describing the edge/screw character of dislocations and the dislocation arrangement parameter M. The value of d is calculated as $d = m \exp(2.5\,\sigma^2)$, where m is the median and σ^2 is the variance of the log-normal crystallite size distribution.

3. *Ab-initio* calculations of positron lifetimes

Density functional theory was employed for calculations of the lifetimes of positrons trapped at various point defects in bcc Fe lattice. Positron density was calculated within the so-called standard scheme [42] employing the atomic superimposition (ATSUP) method [43]. The electron–positron correlation was treated using the local density approximation (LDA) according to the parametrization by Boroński and Nieminen [44]. The calculations were performed in 128 Fe atom based supercells. Point defects (vacancies and vacancy clusters) were modelled simply by removing the corresponding number of atoms from the supercell.

4. Results

4.1. Microstructure evolution from electron microscopy

The development of UFG structure was studied in IF steel samples subjected to various number of HPT revolutions. SEM micrographs of IF steel subjected to 1 (left panels) and 5 (right panels) HPT revolutions are presented in Fig. 2. The first row, i.e.

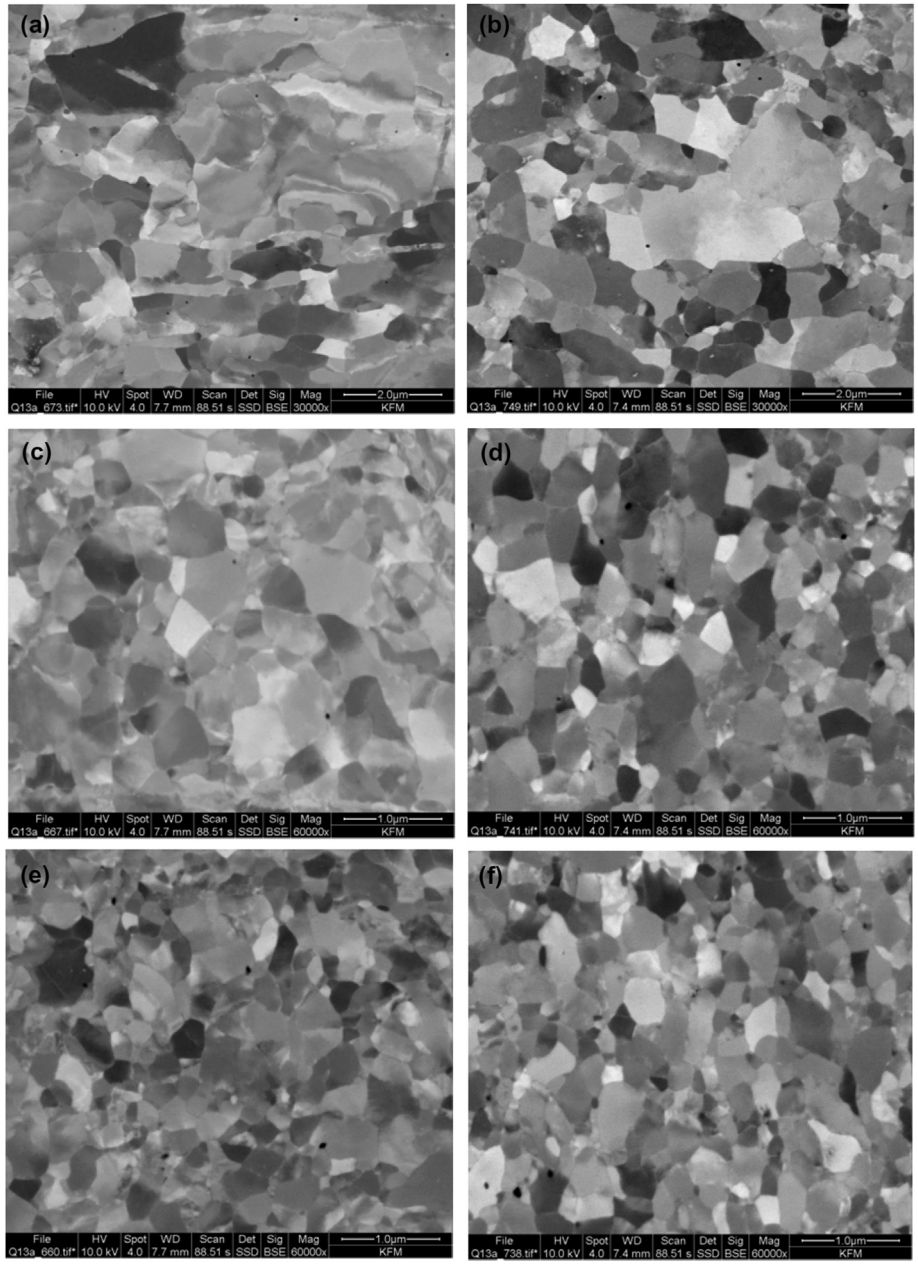

Fig. 2. SEM micrographs (back scattered electrons – channelling contrast) displaying the microstructure in different parts of HPT-deformed specimens subjected to 1 and 5 HPT turns. Left panels $N = 1$: (a) centre $r = 0$, (c) half radius $r = 2.5$ mm, (e) periphery $r = 4$ mm; right panels $N = 5$: (b) centre $r = 0$, (d) half radius $r = 2.5$ mm, (f) periphery $r = 4$ mm.

Fig. 2a,b, shows the centre of the sample disk ($r = 0$); the second row, i.e. Fig. 2c,d, shows the half radius of the sample ($r = 2.5$ mm); and the last row, i.e. Fig. 2e,f shows the microstructure at the periphery ($r = 4$ mm). Obviously the grains in the centre of the sample are coarser than those in the half radius and at the periphery. This difference remains clearly visible even after 5 HPT revolutions.

Fig. 3 shows EBSD map of IF steels deformed by 1 (Fig. 3a,c,e) and 5 HPT (Fig. 3b,d,f) revolutions. The microstructure in the centre of the specimen subjected to 1 HPT revolution (Fig. 3a) has a bimodal character consisting mostly of bands of elongated grains and subgrains. Fine grains/subgrains with the size below 1 μm coexist with coarse grains with the diameter above 5 μm. This testifies that grain fragmentation has already started even in the central region of the sample disk but original large grains are still present in the microstructure. On the other hand, refined equiaxed grain structure with the mean grain size around 0.5 μm is clearly seen at the periphery (Fig. 3e). Further HPT straining up to 5 turns did not result in additional decrease of the grain size at the periphery (Fig. 3f). However, at the half radius (Fig. 3d) and in the centre (Fig. 3b) the grains were further refined.

Grain size distributions determined by EBSD in the samples subjected to various numbers of HPT turns are presented in Fig. 4a–e. For each sample the grain size distribution was determined in the centre of the sample disk ($r = 0$), at the half-radius ($r = 2.5$ mm) and at the periphery ($r = 4$ mm). For all samples studied the grain size distribution has approximately a log-normal shape. Best fits of grain size histograms by a log-normal distribution are plotted by solid lines in the figure. The samples deformed by 1/4 and 1/2 HPT revolutions exhibit rather broad size distribution of grain sizes and still contain a considerable fraction of coarse grains

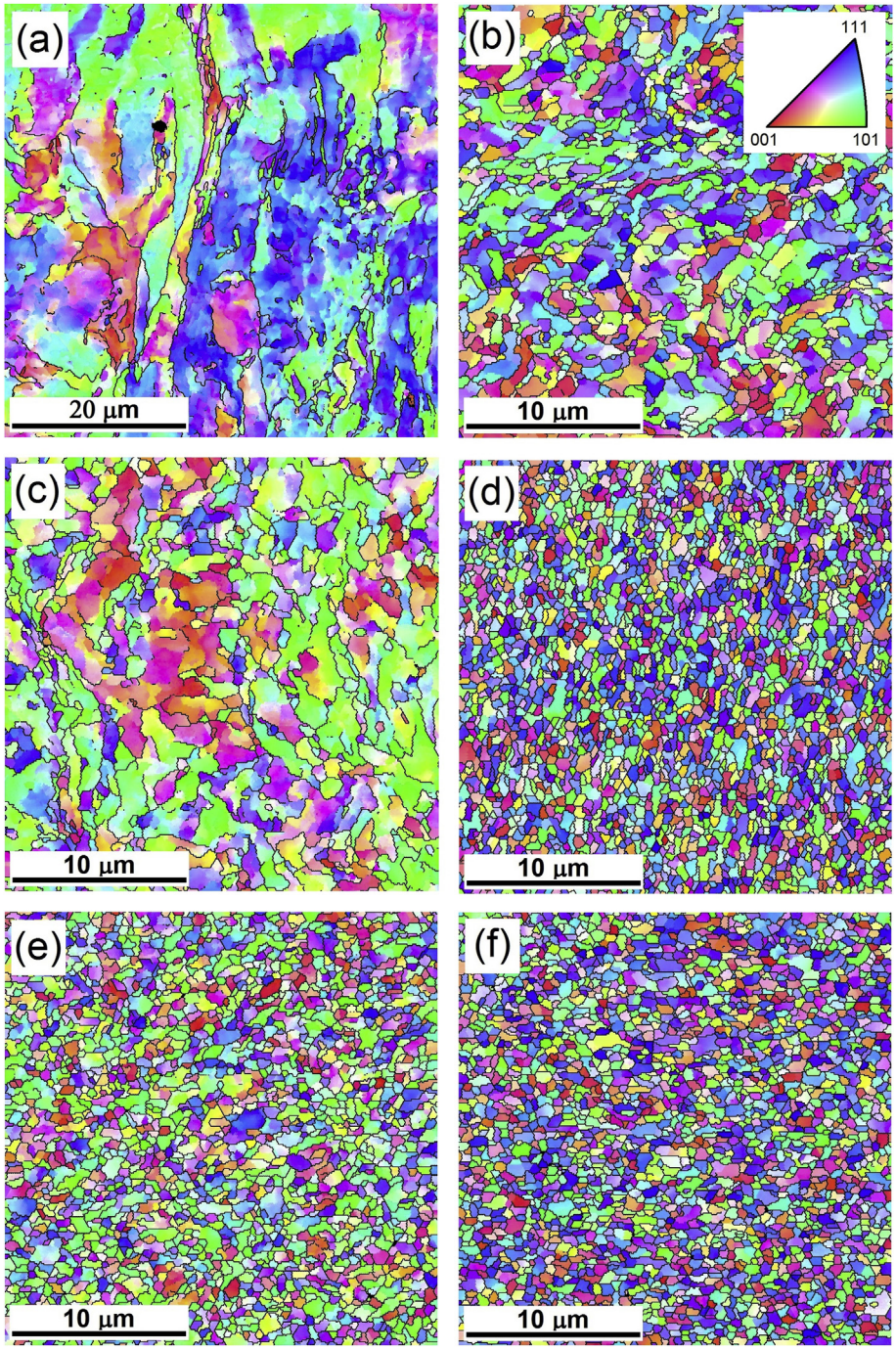

Fig. 3. EBSD maps of HPT specimens deformed by one revolution ($N = 1$), left panels and by 5 revolutions ($N = 5$), right panels. The samples were examined in the centre ($r = 0$), half-radius ($r = 2.5$ mm) and at the periphery ($r = 4$ mm): (a) $N = 1$, centre, (b) $N = 5$, centre, (c) $N = 1$, half-radius, (d) $N = 5$, half-radius, (e) $N = 1$, periphery and (f) $N = 5$, periphery.

with a diameter larger than 5 μm. With increasing strain the grain size distribution becomes sharp indicating that the microstructure consists of refined grains most of them with a size below 1 μm. The narrowing of grain size distribution occurs first at the periphery (after 1 HPT revolution, see Fig. 4c) then also at the half-radius (after 3 HPT revolutions, see Fig. 4d) and finally in the centre. One can see in Fig. 4d that the grain size distribution at the half-radius becomes practically the same as at the periphery after 3 HPT turns. Nevertheless, the grain size distribution in the centre is still broader than at the half-radius and at the periphery even after 5 HPT turns, see Fig. 4e. The development of the mean grain size D (i.e. the mean value of the grain size distribution determined by EBSD) is plotted in Fig. 4f. The dependence of the mean grain size on the number of HPT revolutions can be well described by an exponential decaying function. At the beginning of HPT straining the mean grain size strongly decreases due to substantial grain refinement by SPD. The grain refinement becomes saturated and the mean grain size becomes $D \approx 0.5$ μm first at the periphery (after a single HPT turn) and then at the half-radius (after 3 HPT revolutions). In the centre the grain refinement seems to be saturated after 3 HPT turns as well, but the mean grain size is slightly higher ($D \approx 0.6$ μm) than at the half-radius and the periphery. This

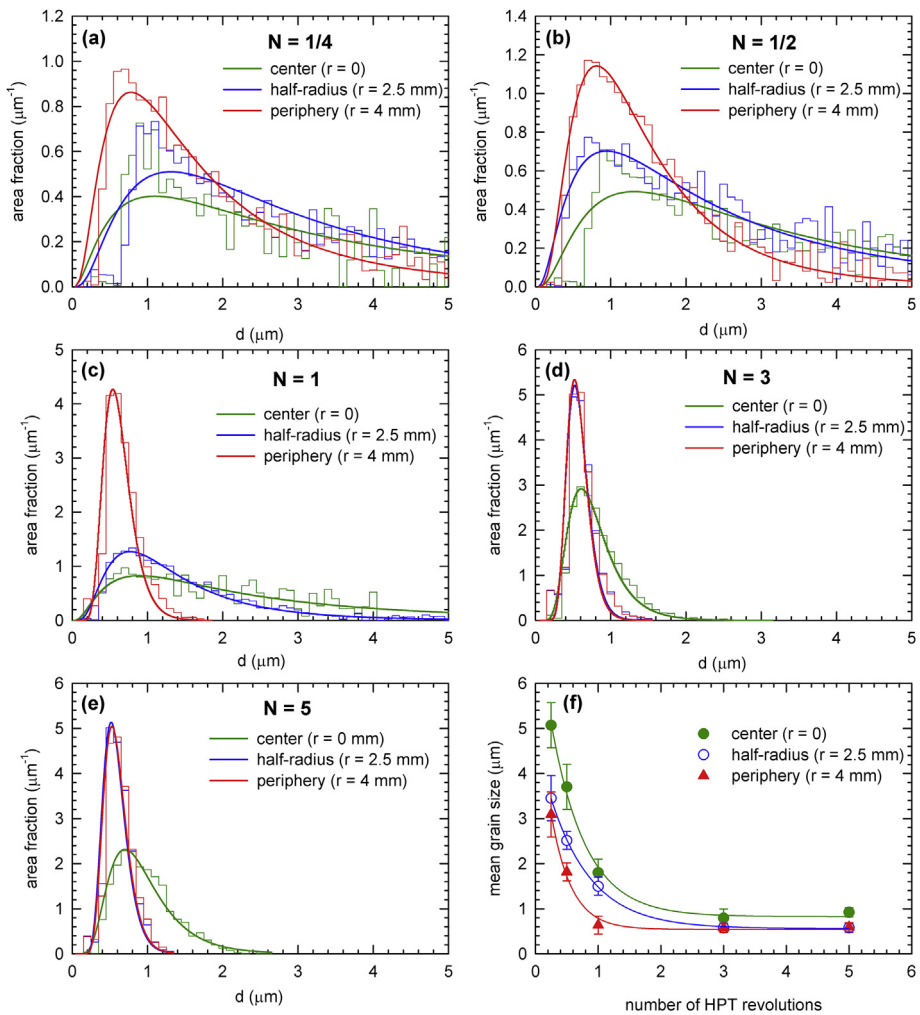

Fig. 4. Grain size distributions of specimens subjected to various number N of HPT revolutions determined by EBSD: $N = 1/4$ (a), $N = 1/2$ (b), $N = 1$ (c), $N = 3$ (d), $N = 5$ (e). For each sample the grain size was determined in the centre of the sample disk ($r = 0$), at the half-radius ($r = 2.5$ mm) and at the periphery ($r = 4$ mm). The solid lines show fits of the experimental histograms by a log-normal distribution. The last panel (f) shows the mean grain size as a function of the number of HPT revolutions.

is due to broader grain size distribution in the centre containing still a considerable portion of grains with the size higher than 1 μm.

The fractions of high angle grain boundaries (HAGBs) with misorientation of neighbouring grains higher than 15° was determined by EBSD and are plotted in Fig. 5 as a function of the number of HPT turns. The fraction of HAGBs significantly increases with increasing the number of HPT revolutions. This increase is the most rapid at the periphery subjected to the highest strain while at the half-radius and in the centre it is more gradual. After sufficient number of HPT revolutions HAGBs represent the dominating type of grain boundaries. In the sample deformed by 5 HPT turns the fraction of HAGBs is approximately 80% at the periphery and the half-radius.

4.1.1. X-ray diffraction

Fig. 6 shows an example of X-ray diffraction pattern measured in the centre of the IF steel sample subjected to 3 HPT revolutions. The theoretical function obtained by CMWP fitting is plotted in Fig. 6 by a solid line. The size of the X-ray beam spot on the sample surface was about 2×0.2 mm^2. As the longer dimension of the beam spot (2 mm) was smaller than the radius of the disks (5 mm) only by a factor of 2.5, the microstructure could not be studied in the region near the periphery of the samples. Therefore, XLPA measurements

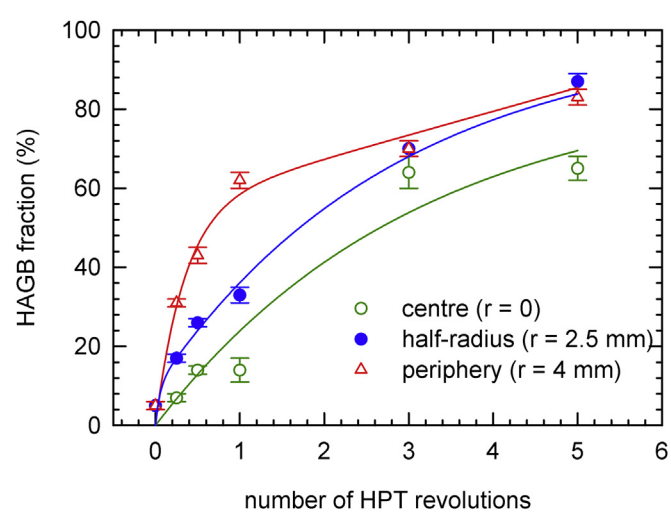

Fig. 5. The fraction of HAGBs (missorientation > 15°) determined by EBSD in the centre, half-radius and periphery of the sample disk plotted as a function of the number of HPT revolutions.

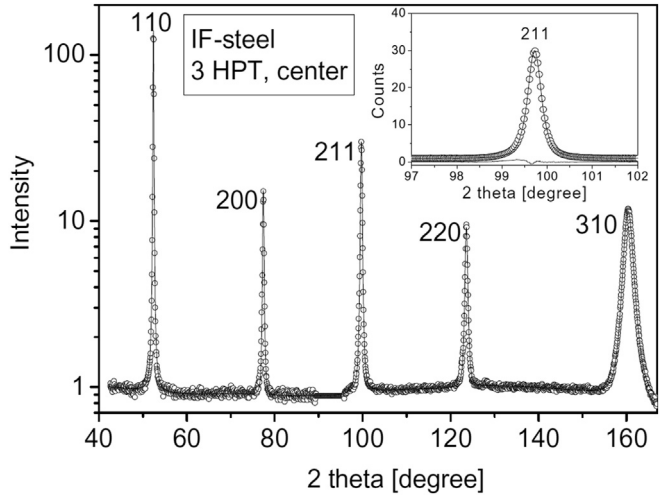

Fig. 6. An example of X-ray diffraction pattern for the IF steel sample deformed by 3 HPT turns. The diffraction pattern was measured in the centre of the sample disk. The open circles and the solid line represent the measured data and the theoretical curves obtained by CMWP fitting, respectively. The intensity is plotted in logarithmic scale. The inset shows a part of the diffractogram in larger magnification. In the inset the intensity is plotted in linear scale and the difference between the measured and the fitted patterns is shown at the bottom.

were carried out only in the centre ($r = 0$) and the half-radius ($r = 2.5$ mm) of the disks as shown schematically in Fig. 7.

The development of the mean crystallite size d with increasing the number of HPT revolutions is plotted in Fig. 8. The mean crystallite size was determined by XLPA in the centre of the sample disk and at the half radius. One can see in the figure that the mean crystallite size at the half radius becomes saturated at the value $d \approx 87$ nm already at the beginning of HPT straining. In the centre d gradually decreases with increasing the number of HPT revolutions and becomes saturated after ~3 HPT revolutions.

The mean dislocation densities ρ_D determined by XLPA in the centre and at the half-radius of HPT deformed samples are plotted in Fig. 9. The dislocation density ρ_D was found to strongly increase with increasing the number of HPT turns. At the half-radius ρ_D becomes saturated at $\approx 8 \times 10^{14}$ m^{-2} already after 1/4 HPT revolution. In the central region the increase of ρ_D is gentler and its

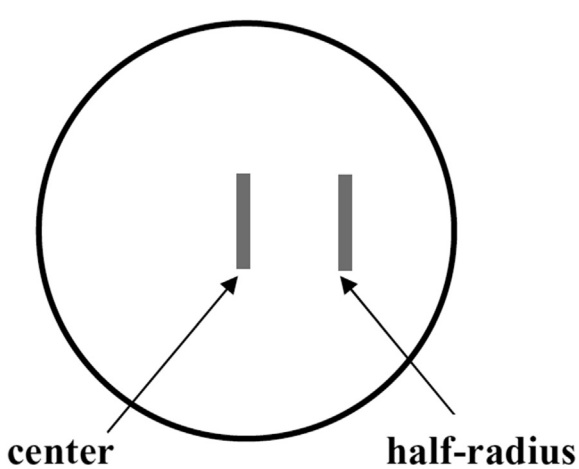

Fig. 7. Schematic depiction of the position of X-ray beam spot on HPT-deformed sample disk. The X-ray diffraction measurements were performed in the centre of the sample disk ($r = 0$) and at the half radius ($r = 2.5$ mm). The size the beam spot was 2×0.2 mm^2.

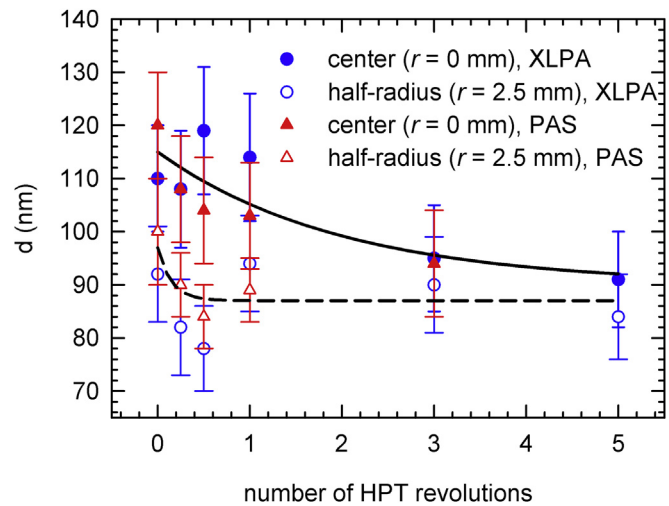

Fig. 8. The mean crystallite size d determined by XLPA (circles) and by PAS (triangles) in the centre (full symbols) and at the half-radius (open symbols) of the IF steel samples deformed by various numbers of HPT revolutions.

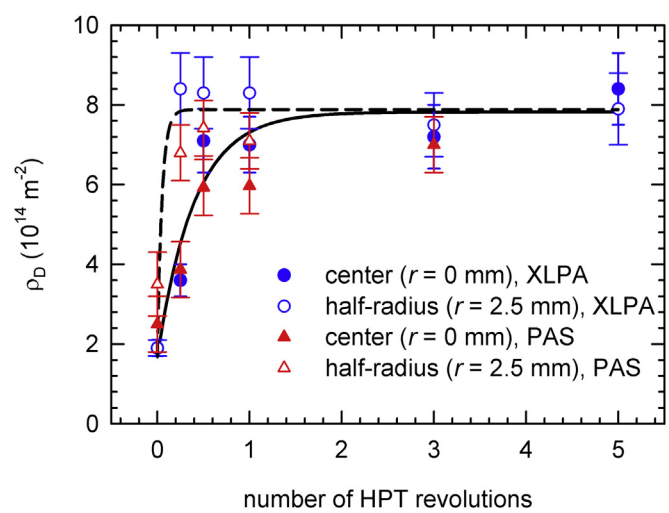

Fig. 9. The development of the mean dislocation density ρ_D during HPT processing. The mean dislocation density was determined by XLPA (circles) and by PAS (triangles) in the centre (full symbols) and at the half-radius (open symbols) of HPT-deformed sample disk.

saturation occurs only in samples deformed by more than a single HPT turn.

The screw/edge character of dislocations was evaluated using XLPA. The theoretical values of the parameter q for the most common pure edge and screw dislocations in bcc structure with the Burgers vector 1/2 < 111> and the slip plane {110} are 1.28 and 2.67, respectively [45]. For a dislocation structure having mixed character the value of q is between these limiting cases. For the material which was only pressed without any torsional rotation ($N = 0$), the experimental values of q at both the centre and the half-radius obtained from the CMWP fitting are between 1.8 and 1.9. These values are close to the arithmetic average of the theoretical values for pure edge and screw dislocations. Hence, the character of dislocations in the sample $N = 0$ is mixed and the fraction of screw dislocations is $f_{screw} \approx 0.6$. At the same time, the samples torsioned by HPT ($N > 0$) exhibit lower q values between 1.4 and 1.6, indicating that the dislocation structure has rather edge character and f_{screw} decreased to $\approx$ 0.2. The behaviour of the dislocation

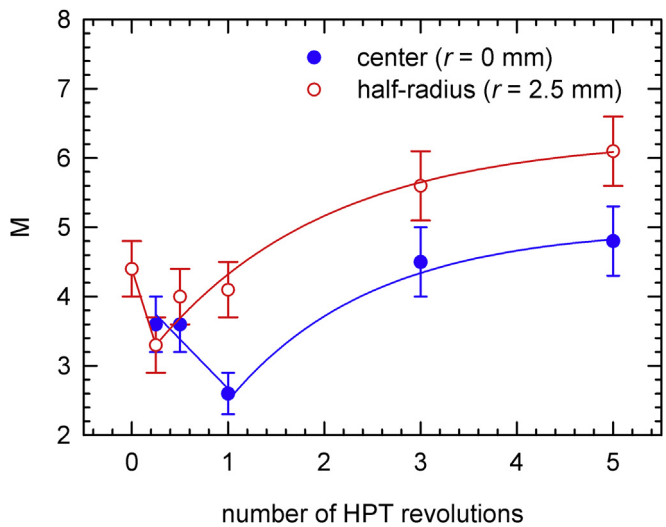

Fig. 10. The dislocation arrangement parameter *M* plotted as a function of the number of HPT revolutions. The *M* parameter was determined by XLPA in the centre (full symbols) and at the half-radius (open symbols) of HPT deformed sample disk.

arrangement parameter *M* during HPT processing is shown in Fig. 10. In the centre *M* first decreases with increasing the number of HPT revolutions up to 1 turn, then it gradually increases for 3 and 5 revolutions. The reduction of *M* indicates that the dislocations formed during HPT are rearranged into low energy configurations (e.g. LAGBs or dipoles). When the dislocation density saturates, *M* starts to increase again. This can be explained by the easier annihilation of dislocations in dipoles. The newly formed dislocations replace the annihilated dislocations. Similar trend can be observed at the half-radius region, but since saturation of dislocation density occurs earlier the increase of *M* starts already after 1/4 HPT revolution.

4.2. Positron annihilation spectroscopy

The LT studies of IF steel specimens deformed by HPT were performed in the centre of the sample disk ($r = 0$) and at the half-radius region ($r = 2.5$ mm). Fig. 11a shows the lifetimes of the exponential components resolved in LT spectra as a function of the number of HPT revolutions. The development of relative intensities of these components is shown in Fig. 11b. The sample which was only pressed ($N = 0$) exhibits two-component LT spectrum. The shorter component with lifetime τ_1 can be attributed to free positrons while the longer component with lifetime $\tau_2 \approx 155$ ps comes from positrons trapped at defects. The lifetime τ_2 falls into the range reported for positron trapped at dislocations in Fe [46] and steels [47–49]. It has to be mentioned that the dislocation line itself represents only a shallow positron trap unable to confine positron at room temperature. According to generally accepted model proposed by Smedskjaer et al. [50] positron trapping at dislocations is a two-state process. Once a positron arrives at the core of a dislocation, it diffuses quickly along the dislocation line until it finds a vacancy attached to the dislocation or a jog at the dislocation where it is finally trapped and annihilated [50–52]. A vacancy is attracted to the compressed region around dislocation line and is squeezed by the compressive elastic field produced by the dislocation. As a consequence, the lifetimes of positrons trapped at dislocations are usually slightly shorter than those for isolated vacancies. Since atomic relaxations around edge and screw dislocation differ the positron lifetimes for edge and screw dislocations differ as well. Detailed LT investigations of deformed Fe performed by Park et al. [46] revealed that the lifetime of positrons trapped at screw dislocations is $\tau_{\mathrm{screw}} = 142$ ps, while that for edge dislocations is $\tau_{\mathrm{edge}} = 165$ ps. Hence, the lifetime $\tau_2 \approx 155$ ps measured here for HPT deformed IF steels can be attributed to positrons trapped at a mixture of screw and edge dislocations. The fraction of screw dislocations f_{screw} can be estimated from the lifetime τ_2 using the relation

$$f_{screw} \approx \frac{\tau_{edge} - \tau_2}{\tau_{edge} - \tau_{screw}}. \quad (2)$$

Using Eq. (2) one can estimate the fraction of screw dislocations $f_{screw} \approx 0.4$, i.e. dislocations in HPT-deformed IF steels have mainly edge character. Note, that similar result was obtained by XLPA investigations. During HPT straining the lifetime τ_2 remains approximately constant which testifies that dislocation character remains approximately the same.

The LT spectra of samples strained by HPT ($N > 0$) contain an additional long-lived component with lifetime τ_3 gradually increasing with the number of HPT turns from ≈340 to ≈ 380 ps. These lifetime values correspond to larger point defects, namely

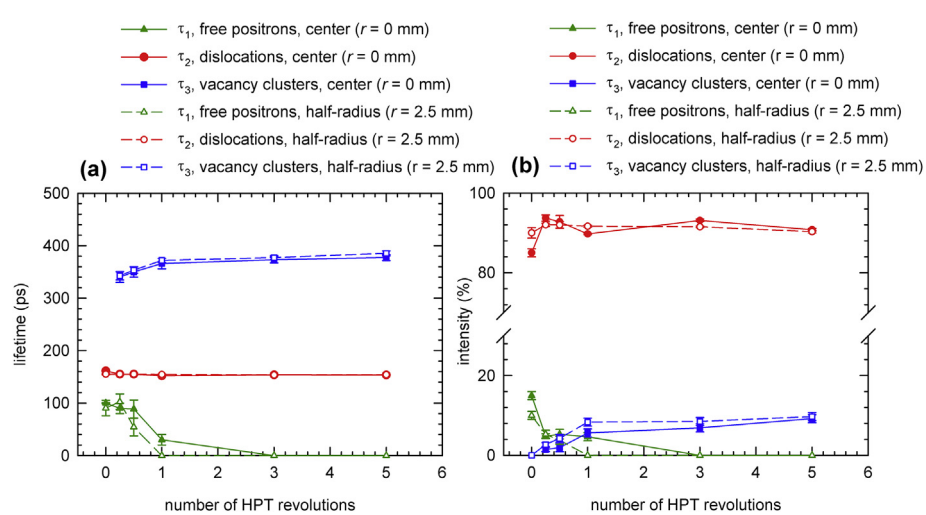

Fig. 11. Results of LT investigations of IF steels deformed by HPT: lifetimes of exponential components (a) and their relative intensities (b) plotted as a function of the number of HPT revolutions. Data measured in the centre of the sample disk ($r = 0$) and at the half-radius ($r = 2.5$ mm) are plotted by full and open symbols, respectively.

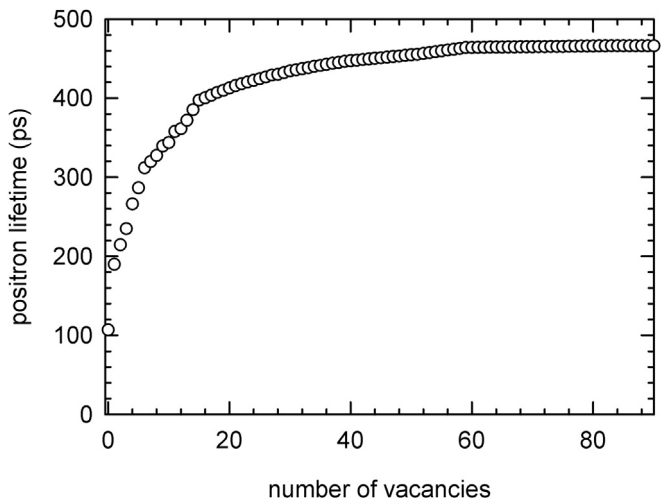

Fig. 12. Calculated lifetimes of positrons trapped in vacancy clusters of various sizes in bcc Fe lattice.

vacancy clusters formed by agglomeration of deformation-induced vacancies [28]. Since vacancies in Fe are mobile at room temperature [53], vacancies introduced by SPD either disappear by diffusion to sinks at grain boundaries or are bound to dislocations or agglomerate with other vacancies forming vacancy clusters which are more stable and survive in the sample at room temperature. Agglomeration of deformation-induced vacancies into clusters is supported by the fact that during movement of jogs at screw dislocations or climbing of edge dislocations vacancies are introduced in chains and thereby can merge together relatively easily.

It should be mentioned that in addition to vacancies interstitials were most probably also formed by stress-induced motion of jogs at screw dislocations and climbing of edge dislocations despite the fact that the formation energy of an interstitial in bcc Fe lattice is about four times higher than that for a vacancy [54]. Deformation-induced interstitials may also agglomerate and form interstitial clusters or interstitial loops. However these interstitial defects are not detectable by positron annihilation spectroscopy since they contain no free volume and repel positrons.

Ab-initio theoretical modelling was employed to determine the average size of vacancy clusters in HPT deformed IF steels. Fig. 12 shows the calculated lifetimes for positrons trapped at vacancy clusters of various sizes in bcc Fe lattice, i.e. vacancy clusters consisting of various numbers of vacancies. For small vacancy clusters the lifetime of trapped positrons strongly increases with increasing the cluster size while for larger clusters the lifetime gradually saturates. From comparison of the experimental lifetime τ_3 with theoretical calculations one can conclude that the vacancy clusters in IF steel deformed by 1/4 HPT turn consist *on average* of 9 vacancies. With increasing the number of HPT revolutions the average size of vacancy clusters grows up to 14 vacancies.

From inspection of Fig. 11b it becomes clear that the intensity I_3 of the vacancy cluster component gradually increases at the expense of the intensity I_1 of the free positron component testifying the rising concentration of vacancy clusters. The increase of the concentration of vacancy clusters at the half-radius region is faster than in the centre region due to higher strain. The density of dislocations increases as well, mainly in the beginning of HPT straining leading to an increase of the intensity I_2. When the density of defects becomes so high that practically all positrons are annihilated from a trapped state (so called saturated trapping), the free positron component cannot be resolved in LT spectrum anymore, i.e. $I_1 = 0$. One can see in Fig. 11b that it happened at the half-radius region after a single HPT revolution while in the centre the increase of defect density is slower and the saturated trapping occurred after 3 HPT turns.

The mean crystallite size d and the mean dislocation density ρ_D were determined from LT data using DTM and are plotted as a function of the number of HPT turns in Figs. 8 and 9, respectively. One can see in the figures that both d and ρ_D determined by PAS are in a very good agreement with the values obtained by XLPA. Note that DTM can be applied for the determination of d and ρ_D only when the free positron component was resolved in LT spectrum, i.e. only when saturated positron trapping did not occur.

Results of DB mapping are presented in Fig. 13. The dependencies of the S-parameter on the radial distance r from the centre of the samples subjected to various numbers of HPT revolutions are plotted in Fig. 13a. The S-parameter values strongly increase with increasing strain and saturate after a single HPT revolution. In the samples deformed by 1/4, 1/2 and 1 HPT turn one can see a gradual increase of S from the centre towards periphery of the sample disk. The development of the S-parameter in the centre, at the half-radius and at the periphery is plotted in Fig. 13b. A strong increase of S at the beginning of HPT straining followed by saturation after a single HPT revolution is clearly seen in this figure. The S-parameter values in the centre are slightly lower than those at the half-radius and the latter values are lower than S values at the periphery except that of the sample deformed by 5 HPT revolutions, where the S parameter becomes practically uniform across the whole sample. This behaviour of the S-parameter is in accordance with the results of LT studies.

4.3. Microhardness

The homogeneity of UFG structure was also studied by HV testing. Fig. 14 shows colour coded maps of HV distributions across the IF steel sample disk subjected to various number of HPT revolutions. One can see in the figure that HV distribution has axial symmetry with respect to the centre of the sample disk. The radial dependence of HV was constructed for each sample by averaging the HV values measured at the same distance from the centre and is plotted in Fig. 15. The sample $N = 0$ exhibits almost uniform distribution of HV across the whole sample disk. HV is slightly lowered in the centre and an apparent increase of HV was observed at the edge due to out-flow of material pressed between the anvils in the semi-constrained design. This hardness variation along the disk radius is in agreement with recent finite element modelling calculations [55]. HPT straining ($N > 0$) leads to a remarkable hardening reflected by an increase of HV values, see Fig. 14b–f. The increase of HV is most pronounced at the periphery where HV is almost saturated already after a single HPT revolution, see Fig. 15. In the regions closer to the centre of the sample, HV increases more gradually. This is obviously due to a non-uniform strain increase from the centre of the sample towards the periphery according to Eq. (1). As a consequence the HV profiles across the samples deformed by 1/4, 1/2 and 1 HPT revolutions become strongly non-uniform, see Fig. 14b,c,d and Fig. 15. In samples deformed by more than 1 HPT revolution HV becomes saturated not only at the periphery but also at smaller distances from the centre, i.e. the region of saturated HV gradually extends from the periphery towards the centre, see Figs. 14e,f and 15. The centre of the sample disk, however, exhibits remarkably lower HV even after 5 HPT revolutions, see Figs. 14f and 15.

5. Discussion

The development of the mean grain size D determined from EBSD experiments with increasing equivalent strain calculated

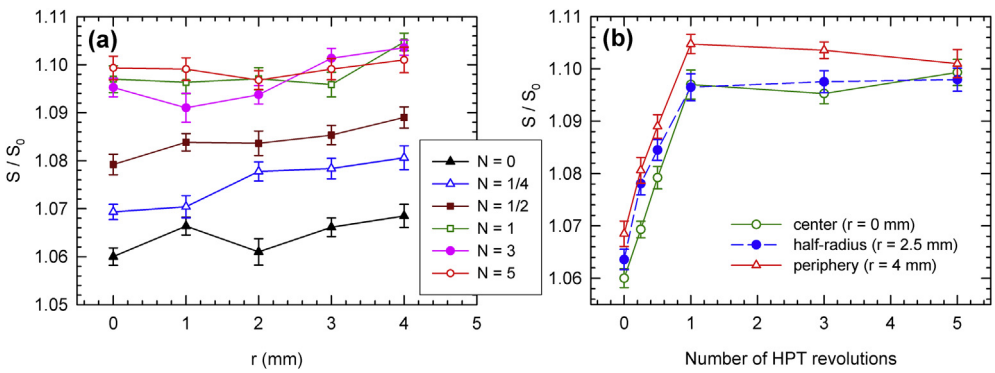

Fig. 13. Results of DB mapping of IF steels deformed by HPT: the dependence of the *S*-parameter on the radial distance *r* from the centre of the sample disk (a); the development of the *S*-parameter in the centre, at the half radius and at the periphery with increasing number of HPT revolutions (b). Note that *S* values at the half radius ($r = 2.5$ mm) were calculated as the arithmetic average of the *S* parameters measured at the radial distances $r = 2$ and 3 mm.

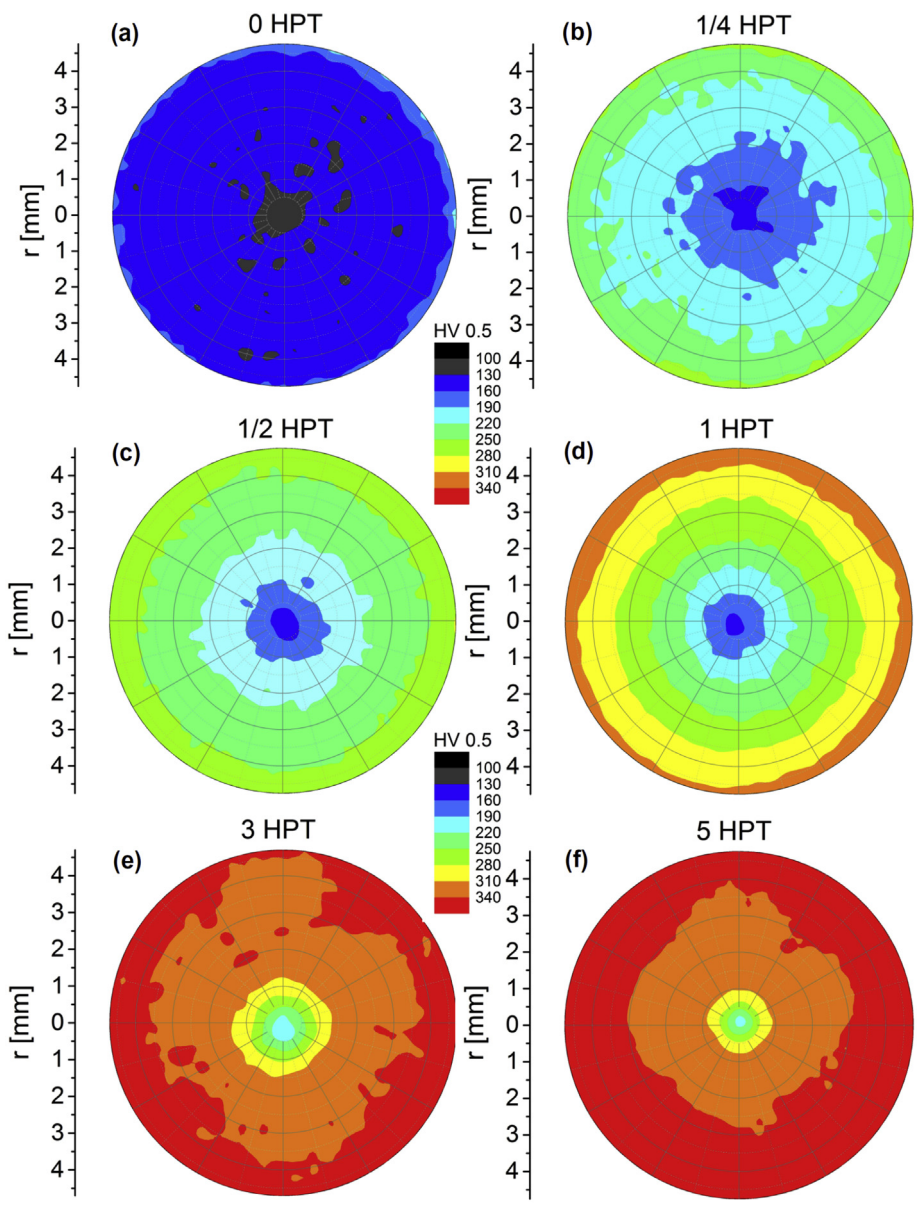

Fig. 14. Colour coded HV maps of IF steel disks subjected to various number of HPT revolutions. The sample $N = 0$ was only pressed between the anvils of the HPT machine without any rotation. (For interpretation of the references to colour in this figure legend, the reader is referred to the web version of this article.)

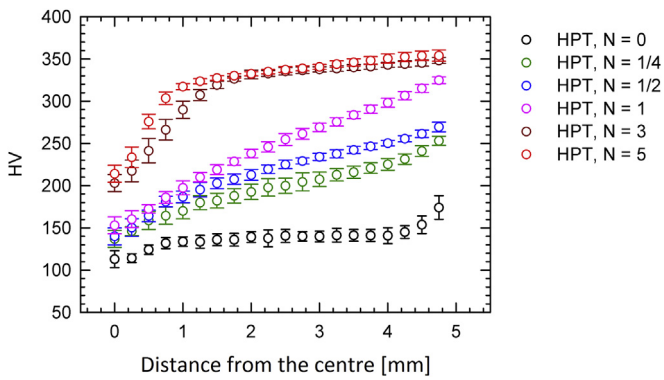

Fig. 15. Dependences of HV on the radial distance r from the centre of sample disks deformed by HPT using various numbers of turns.

from Eq. (1) is plotted in Fig. 16. From inspection of Fig. 16 it becomes clear that the mean grain size decreases approximately linearly with logarithm of the equivalent strain and becomes saturated at $D \approx 0.58$ μm in the samples subjected to the equivalent strain $e_{equiv} > 15$. Hence, the dependence of the mean grain size D on the equivalent strain e_{equiv} can be expressed as

$$D[\mu\ \mathrm{m}] = \begin{cases} a_D - b_D \log e_{equiv} & \text{for } e_{equiv} \le 15 \\ 0.58 & \text{for } e_{equiv} > 15 \end{cases}. \quad (3)$$

The coefficients $a_D = (4.1 \pm 0.2)$ μm and $b_D = (2.98 \pm 0.08)$ μm were obtained by linear regression of the data in Fig. 16.

The mean size of dislocation cells d determined by XLPA and PAS is plotted in Fig. 17 as a function of the equivalent strain e_{equiv}. The figure includes data for all regions where both the cell size d and the dislocation density ρ_D were determined by PAS or XLPA, i.e. in the centre and at the half-radius regions of the samples subjected to various number of HPT revolutions. Note that for $e_{equiv} > 10$ saturated positron trapping at defects takes place and d cannot be determined by PAS anymore. From the inspection of Fig. 17 it becomes clear that there is an excellent agreement between the d values determined by PAS and XLPA. The mean crystallite size d decreases with increasing strain and becomes saturated at $d \approx 87$ nm for $e_{equiv} > 10$.

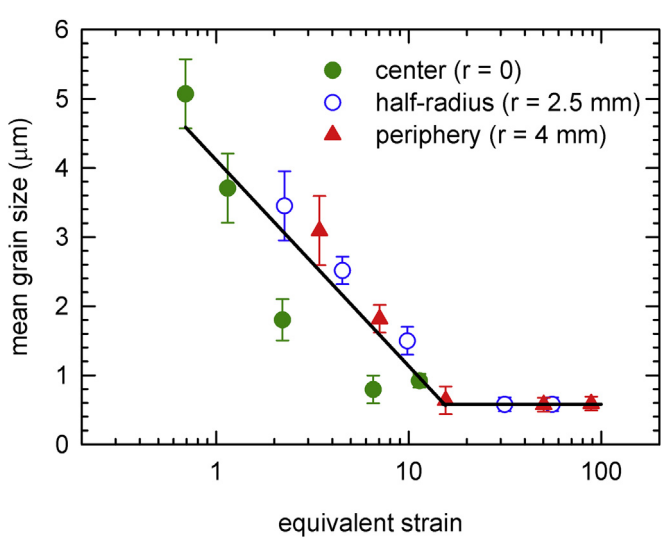

Fig. 16. The mean grain size determined by EBSD in the centre, at the half-radius and at the periphery of the sample disk plotted as a function of the equivalent strain.

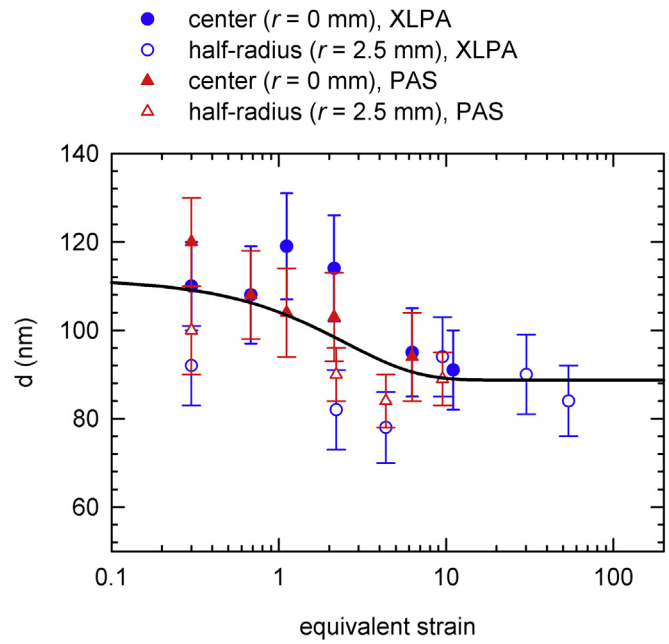

Fig. 17. The mean crystallite size d in the centre (full symbols) and at the half-radius (open symbols) of the sample disk determined by XLPA (circles) and PAS (triangles) plotted as a function of the equivalent strain.

Fig. 18 shows the mean dislocation density ρ_D plotted as a function of the equivalent strain e_{equiv}. There is again an excellent agreement between the ρ_D values determined by PAS and XLPA. One can see in the figure that ρ_D first increases with e_{equiv} and becomes saturated at $\rho_D \approx 8 \times 10^{14}$ m^{-2} for $e_{equiv} \ge 3$. The dependence of ρ_D on the equivalent strain can be well described by a function exponentially rising to saturation

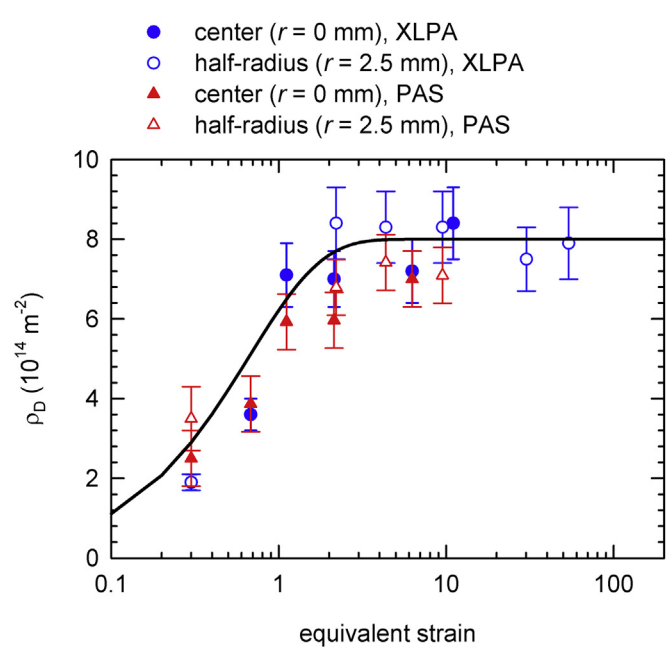

Fig. 18. The mean dislocation density ρ_D in the centre (full symbols) and at the half-radius (open symbols) of the sample disk determined by XLPA (circles) and PAS (triangles) plotted as a function of the equivalent strain.

$$\rho_D = a_\rho \lfloor 1 - \exp(-b_\rho e_{equiv}) \rfloor, \quad (4)$$

which is plotted in Fig. 18 by a solid line. The coefficients $a_\rho = (8.0 \pm 0.4) \times 10^{14}\ \mathrm{m}^{-2}$ and $b_\rho = (1.5 \pm 0.2)$ led to the best agreement of Eq. (4) with the experimental data.

Overviewing the evolution of the different microstructure features, it can be concluded that first the dislocation density saturates ($e_{equiv} \approx 3$), then the dislocation cell size reaches its minimum value ($e_{equiv} \approx 10$), finally the grain size gets saturated ($e_{equiv} \approx 15$) with increasing the equivalent strain.

In Fe bcc lattice screw dislocation core is dissociated into a non-planar configuration [56]. This makes annihilation of screw dislocations more difficult than edge ones and dislocations remaining in deformed ferritic steels have usually more screw character [14,57]. In contrast here both XLPA and PAS investigations consistently showed that dislocations in HPT deformed samples have mainly edge character. This might be caused by a high hydrostatic pressure during HPT processing which considerably retards the migration of vacancies representing the basic mechanism of climb of edge dislocations.

High pressure-induced slow down diffusion and consequently suppressed recovery of dislocations was firstly suggested by Valiev et al. [58] based on his study of the microstructure development of HPT deformed Armco Fe. Further this effect was analyzed in more detail by Zehetbauer et al. [59]. Vacancy migration is connected to local changing of volume via continuous mass transfer. Under certain hydrostatic pressure p this requires extra work $p\Omega$, where Ω is the vacancy migration volume [59–61]. As a consequence the effective vacancy migration enthalpy increases as $H_m(p) = H_m(p = 0) + p\Omega$. The pressure-induced enhancement in the vacancy migration enthalpy leads to reduced vacancy migration under high hydrostatic pressure as it was shown by Schafler et al. [60]. Moreover, suppressed migration of vacancies under high pressure hinders annihilation of edge dislocations via climbing [59,60]. This effect has been confirmed experimentally in HPT deformed Cu [60] and Ni [61].

Hence due to suppressed migration of vacancies during HPT processing, the annihilation of edge dislocations became more difficult than the annihilation of screw ones, and consequently the dislocation structure in HPT deformed IF steels obtains rather edge character. The inhibiting effect of the high hydrostatic pressure on the mobility of vacancies can also be supported by the fact that high concentrations of vacancies were found by PAS in HPT deformed samples. The mobility of vacancies is suppressed due to high hydrostatic pressure and their number which can disappear by diffusion to sinks is significantly reduced. As a consequence, a considerable fraction of vacancies remains in the sample agglomerated in small vacancy clusters.

It has to be noted that a high hydrostatic pressure not only suppresses the mobility of vacancies but also increases the vacancy formation enthalpy [62] since excess volume of vacancies must be created against the hydrostatic pressure. *Ab-initio* theoretical calculations for bcc tantalum [63] revealed that the relative increase of the vacancy formation enthalpy in the pressure range 0–50 GPa is ~1% per GPa. Hence, one can estimate that for the pressure of 2.5 GPa used in the present HPT processing of IF-steels the relative increase of the vacancy formation enthalpy is around 3%. Such increase of the vacancy formation enthalpy leads to a considerable reduction of the equilibrium concentration of vacancies. For example under assumption that the vacancy formation enthalpy in Fe is ≈ 1.4 eV [64] at the atmospheric pressure, the room temperature equilibrium concentration of vacancies in Fe subjected to a hydrostatic pressure of 2.5 GPa would be reduced roughly to one fifth of its atmospheric pressure value. However, it has to be emphasized that vacancies introduced by HPT are non-equilibrium vacancies and their concentration exceeds the equilibrium concentration of vacancies at room temperature by many orders of magnitude [16,18,59,61]. Note that a high concentration of deformation-induced vacancies in a concentration on the order of 10^{-3} has been recently reported for HPT deformed nanocrystalline steel obtained by mechanical alloying of iron and graphite [65].

Hence, vacancy formation at high pressures requires more work. This extra work is supplied by the external forces applied in HPT plastic deformation. Indeed, in-situ stress measurements performed during HPT deformation of Cu and Ni [59–61] revealed that the flow stress measured under high hydrostatic pressure is significantly higher than that in the unloaded sample after deformation. The flow stress increases approximately linearly with hydrostatic pressure and its relative increment was found to be ≈ 0.8 and ≈ 1.5 per GPa for Cu and Ni, respectively [59]. Zehetbauer et al. [59] developed a model which explains the pressure-induced increase of the flow stress by three contributions: (i) increase of shear modulus, (ii) excess work required for creation of excess volume defects (e.g. vacancies) and (iii) permanent change in the microstructure. The results of modelling are in very good agreement with experimental data [59]. Hence, the pressure-induced increase of the vacancy formation enthalpy is one contribution leading to an increase of the flow stress during HPT deformation which was observed experimentally in former works [59–61].

Despite the fact that vacancy formation enthalpy is increased, forces applied during HPT deformation provide the extra work required for the formation of excess volume of vacancies. As a consequence, HPT does not yield a reduction of vacancy concentration despite the fact that vacancy formation enthalpy increased rather the impeded migration to sinks results in increased excess vacancy concentration in HPT-deformed materials.

Fig. 19 shows the dependence of HV on the equivalent strain. The HV values for all HPT deformed samples fall on a common 'master curve' describing the dependence of HV on the equivalent strain. From the inspection of Fig. 19 it becomes clear that HV rapidly increases with the equivalent strain up to $e_{equiv} \approx 20$. For higher equivalent strains the increase of HV becomes significantly less pronounced. Note that even HV values in Fig. 19 corresponding to the centres of the sample disks exhibit some increase with increasing number of HPT revolutions. This is mainly due to

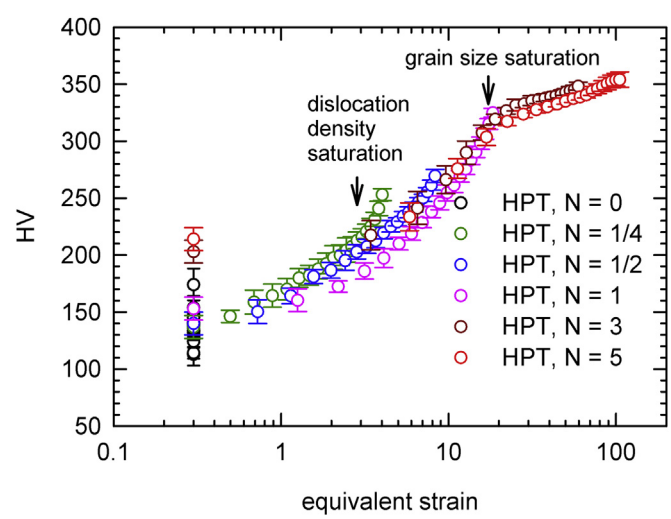

Fig. 19. The development of microhardness with increasing equivalent strain. The equivalent strains where saturation of the dislocation density and the grain size occur are indicated by arrows.

difficulty to locate exactly the centre of the sample, i.e. the HV punctures for the 'centre' were likely made in close vicinity of the centre but not exactly in the centre which is the only point where $e_{equiv} = 0$. In addition, dislocations formed in the vicinity of the centre (where $e_{equiv} \neq 0$) result in stresses in the centre even if $e_{equiv} = 0$, which yields plastic deformation leading to strain hardening.

The yield strength σ was estimated from the HV values using the well known relation $\sigma \approx$ HV/3 and is plotted in Fig. 20 as a function of the equivalent strain. In general the strength of ferritic steels can be influenced by a number of strengthening mechanisms [66], namely: (i) solid solution strengthening, (ii) precipitation strengthening, (iii) dislocation strengthening and (iv) grain size strengthening. Since the composition of IF steels studied here is fixed and also the phase composition remains unchanged during HPT straining, the strength increase of UFG IF steels is caused predominantly by the dislocation and the grain size strengthening. The strength increment caused by dislocations (work hardening) is proportional to the square root of dislocation density [67]. The strength increment due to grain refinement is described by the well known Hall-Petch equation which states that yield strength is proportional to the inverse of the square root of the mean grain size [68]. Assuming a linear addition rule for the different hardening contributions, the yield strength of the UFG IF steels prepared by HPT straining can be expressed as follows

$$\sigma = \sigma_0 + M_T \alpha G b \sqrt{\rho_D} + k \Big/ \sqrt{D}, \tag{5}$$

where σ_0 is the yield strength of the virgin sample prior to HPT straining, M_T is the Taylor factor [69], α is a parameter which describes the strength of dislocation–dislocation interaction [70], G is the shear modulus, b is the length of the Burgers vector and k is the Hall-Petch coefficient describing the strength of the grain boundary resistance [68]. The development of D and ρ_D with increasing strain is described by Eqs. (3) and (4), respectively. Hence, by inserting Eqs. (3) and (4) into Eq. (5), one obtains the dependence of σ on the equivalent strain e_{equiv}. This dependence was fitted to the experimental points of Fig. 20 using the coefficients σ_0, $M_T\alpha Gb$ and k as fitting parameters. The model function calculated by Eq. (5) is plotted in Fig. 20 by a thick solid line. One can see in the figure that the model function is in good agreement with experimental points up to $e_{equiv} \approx 15$. The separate contributions of dislocation and grain size strengthening are plotted in Fig. 20 by thin solid and dashed line, respectively. The coefficients $\sigma_0 = (120 \pm 30)$ MPa, $M_T\alpha Gb = (120 \pm 30) \times 10^{-7}$ MPa m and $k = (530 \pm 10)$ MPa μm$^{1/2}$ were obtained from fitting. Using the Burgers vector $b = a/2\ \langle 111 \rangle \approx 2.5$ Å, the shear modulus of ferritic steel $G \approx 80$ GPa [71] and assuming a random texture characterized by the average Taylor factor $M_T \approx 3$ [69], one obtains the product $M_T Gb = 600 \times 10^{-7}$ MPa m. Comparing it with the coefficient $M_T\alpha Gb$ obtained from fitting yields the parameter $\alpha = (0.20 \pm 0.05)$. This value falls into the range 0.1–0.3 reported for steels in Ref. [72]. The Hall-Petch coefficient k obtained from fitting is in a reasonable agreement with the value $k = 551$ MPa μm$^{1/2}$ determined for ferritic steel by Morrison [73].

The dislocation strengthening saturates at $e_{equiv} \approx 3$ due to saturation of the density of dislocations, c.f. Fig. 18. The grain size strengthening becomes saturated at $e_{equiv} \approx 15$ when the grain size saturates, c.f. Fig. 16. Interestingly, there is an additional, even though, relatively small strengthening effect even at $e_{equiv} > 15$ when both the dislocation density and the grain size are already saturated, see Fig. 20. We propose that this additional strengthening is caused by increasing the volume fraction of HAGBs. The development of the fraction of HAGBs with increasing equivalent strain is presented in Fig. 21. One can see in the figure that the fraction of HAGBs increases approximately linearly with the logarithm of the equivalent strain and does not saturate even for $e_{equiv} \approx 100$. According to the classical pile-up model [74], the Hall-Petch coefficient k can be expressed as

$$k \approx M_T \left(\frac{2Gb\tau_{crit}}{\xi\pi} \right)^{1/2}, \tag{6}$$

where ξ is a geometric factor of order unity and τ_{crit} is the critical shear stress necessary for the transmission of slip across a grain boundary. The Burgers vector b and the shear modulus G are fixed and the Taylor factor M_T remains also approximately unchanged since there is no significant development of texture during HPT processing. However, the critical shear stress is affected by the nature of grain boundaries. Hence, increasing misorientation of {110} planes, which are the primary slip planes in ferritic steels, is expected to increase the critical shear stress τ_{crit} and consequently

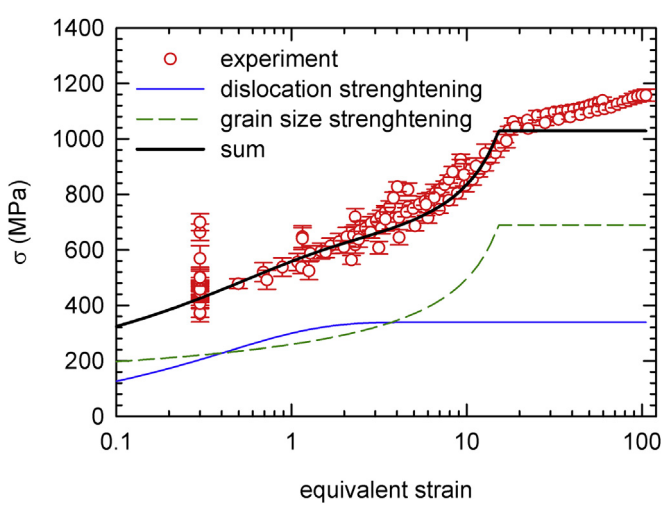

Fig. 20. The yield strength σ for the HPT deformed IF steel samples plotted as a function of the equivalent strain. The thick black solid line shows the model function calculated by Eq. (5) assuming dislocation and grain size strengthening. The contributions of dislocation and grain size strengthening are plotted by thin blue solid line and dashed green line, respectively.

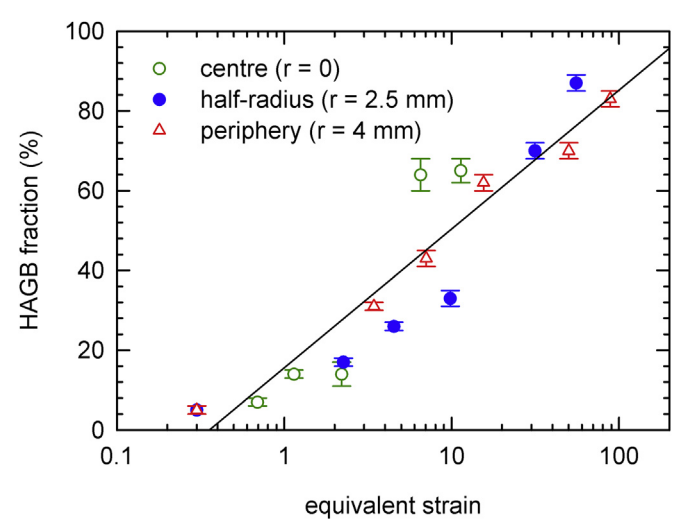

Fig. 21. The development of the fraction of HAGBs at the centre, half-radius, and periphery of the sample disk determined by EBSD as a function of the equivalent strain.

also the Hall-Petch coefficient k. Thus, it is likely that increasing volume fraction of HAGBs in IF steels deformed by HPT leads to an additional strengthening because of gradual increase of the Hall-Petch coefficient.

6. Conclusions

The UFG microstructure in IF steels deformed by HPT was characterized by PAS combined with XLPA and electron microscopy. Results of these investigations can be summarized as follows:

(i) Equiaxed ultra-fine grains are formed in specimens deformed by HPT. Since in torsion deformation the strain increases with the radial distance from the centre of the sample disk towards its periphery the grain refinement at the periphery is faster than in the centre. The grain refinement was saturated at the mean grain size of ~580 nm in the sample deformed up to the equivalent strain $e_{equiv} \approx 15$. The refined grains consist of smaller sub-grains (dislocation cells) separated by dislocation walls.

(ii) The results obtained by XLPA and PAS are mutually consistent. There is an excellent agreement between the mean cell size and the mean dislocation density determined by PAS and XLPA for HPT deformed steels. Hence the combination of PAS and XLPA is beneficial for characterization of UFG microstructure. Both these techniques are capable of determination of the mean size of dislocation cells, the edge/screw character of dislocations and the mean dislocation density. In addition PAS is sensitive also to vacancy-like defects.

(iii) The density of dislocations strongly increases during HPT processing and becomes saturated at the equivalent strain $e_{equiv} \approx 3$. Moreover, non-equilibrium vacancies were created by severe plastic deformation. The high hydrostatic pressure used in HPT processing retarded considerably the vacancy migration and suppressed the recovery of vacancies by diffusion into sinks at grain boundaries. As a consequence considerable fraction of deformation-induced vacancies agglomerated into small clusters consisting of 9–14 vacancies as identified by PAS.

(iv) The strength of IF steels deformed by HPT increases due to dislocation strengthening and also due to grain size strengthening. The dislocation and grain size strengthening is saturated at $e_{equiv} \approx 3$ and 15, respectively. Further straining leads to an additional moderate strengthening due to increasing fraction of HAGBs leading to a higher Hall-Petch coefficient.

Acknowledgement

This work was financially supported by the Czech Science Foundation under the project GB14-36566G. J.C. acknowledges financial support from the Czech Science Foundation under the project P108/13/0943S. H.S.K.ś work was supported by the National Research Foundation of Korea (NRF) grant funded by the Korea government (MSIP) (No. 2014R1A2A1A10051322). J.G. acknowledges financial support by the Hungarian Scientific Research Fund, OTKA, Grant No. K-109021.

References

[1] R.Z. Valiev, Y. Estrin, Z. Horita, T.G. Langdon, M.J. Zehetbauer, Y.T. Zhu, Producing bulk ultrafine-grained materials by severe plastic deformation, JOM 58 (2006) 33–39.
[2] R.Z. Valiev, R.K. Islamgaliev, I.V. Alexandrov, Bulk nanostructured materials from severe plastic deformation, Prog. Mater Sci. 45 (2000) 103–189.
[3] H.S. Kim, Y. Estrin, Ductility of ultrafine grained copper, Appl. Phys. Lett. 79 (2001) 4115–4117.
[4] A.P. Zhilyaev, T.G. Langdon, Using high-pressure torsion for metal processing: fundamentals and applications, Prog. Mater Sci. 53 (2008) 893–979.
[5] D.J. Lee, E.Y. Yoon, D.-H. Ahn, B.H. Park, H.W. Park, L.J. Park, Y. Estrin, H.S. Kim, Dislocation density-based finite element analysis of large strain deformation behavior of copper under high-pressure torsion, Acta Mater 76 (2014) 281–293.
[6] A.P. Zhilyaev, G.V. Nurislamova, B.K. Kim, M.D. Baro, J.A. Szpunar, T.G. Langdon, Experimental parameters influencing grain refinement and microstructural evolution during high-pressure torsion, Acta Mater 51 (2003) 753–765.
[7] A.P. Zhilyaev, K. Oh-ishi, T.G. Langdon, T.R. McNelley, Microstructural evolution in commercial purity aluminum during high-pressure torsion, Mater Sci. Eng. A 410–411 (2005) 277–280.
[8] Y. Estrin, A. Molotnikov, C.H.J. Davies, R.J. Lapovok, Strain gradient plasticity modelling of high-pressure torsion, J. Mech. Phys. Solids 56 (2008) 1186–1202.
[9] Y.Z. Tian, X.H. An, S.D. Wu, Z.F. Zhang, R.B. Figueiredo, N. Gaob, T.G. Langdon, Direct observations of microstructural evolution in a two-phase Cu–Ag alloy processed by high-pressure torsion, Scr. Mater 63 (2010) 65–68.
[10] J. Čížek, O. Melikhova, M. Janeček, O. Srba, Z. Barnovská, I. Procházka, S. Dobatkin, Homogeneity of ultrafine-grained copper deformed by high-pressure torsion characterized by positron annihilation and microhardness, Scr. Mater 65 (2011) 171–174.
[11] H.S. Kim, W.S. Ryu, M. Janecek, S.C. Baik, Y. Estrin, Effect of equal channel angular pressing on microstructure and mechanical properties of IF steel, Adv. Eng. Mater 7 (2005) 43–46.
[12] B. Hadzima, M. Janeček, Y. Estrin, H.S. Kim, Microstructure and corrosion properties of ultrafine-grained interstitial free steel, Mater. Sci. Eng. A 462 (2005) 243–247.
[13] F. Wetscher, A. Vorhauer, R. Stock, R. Pippan, Structural refinement of low alloyed steels during severe plastic deformation, Mater. Sci. Eng. A 387 (2004) 809–816.
[14] K. Máthis, T. Krajňák, R. Kužel, J. Gubicza, Structure and mechanical behaviour of interstitial-free steel processed by equal-channel angular pressing, J. Alloys Comp. 509 (2011) 3522–3525.
[15] A. Sarkar, A. Bhowmik, S. Suwas, Microstructural characterization of ultrafine-grain interstitial-free steel by X-ray diffraction line profile analysis, Appl. Phys. A 94 (2009) 943–948.
[16] T. Ungár, E. Schafler, P. Hanák, S. Bernstorff, M.J. Zehetbauer, Vacancy production during plastic deformation in copper determined by in situ X-ray diffraction, Mater. Sci. Eng. A 462 (2007) 398–401.
[17] E. Schafler, G. Steiner, E. Korznikova, M. Kerber, M.J. Zehetbauer, Lattice defect investigation of ECAP-Cu by means of X-ray line profile analysis, calorimetry and electrical resistometry, Mater. Sci. Eng. A 410–411 (2005) 169–173.
[18] B. Oberdorfer, E.-M. Steyskal, W. Sprengel, W. Puff, P. Pikart, Ch. Hugenschmidt, M. Zehetbauer, R. Pippan, R. Würschum, In situ probing of fast defect annealing in Cu and Ni with a high-intensity positron beam, Phys. Rev. Lett. 105 (2010) 146101.
[19] J. Čížek, M. Janeček, O. Srba, R. Kužel, Z. Barnovská, I. Procházka, S. Dobatkin, Evolution of defects in copper deformed by high-pressure torsion, Acta Mater 59 (2011) 2322–2329.
[20] G. Ribárik, J. Gubicza, T. Ungár, Correlation between strength and microstructure of ball-milled Al–Mg alloys determined by X-ray diffraction, Mater. Sci. Eng. A 387 (2004) 343–347.
[21] J. Gubicza, N.Q. Chinh, Gy. Krállics, I. Schiller, T. Ungár, Microstructure of ultrafine-grained fcc metals produced by severe plastic deformation, Curr. Appl. Phys. 6 (2006) 194–199.
[22] M. Janeček, J. Čížek, J. Gubicza, J. Vrátná, Microstructure and dislocation density evolutions in MgAlZn alloy processed by severe plastic deformation, J. Mater. Sci. 47 (2012) 7860–7869.
[23] T. Ungár, J. Gubicza, G. Ribárik, A. Borbély, Crystallite size distribution and dislocation structure determined by diffraction profile analysis: principles and practical application to cubic and hexagonal crystals, J. Appl. Cryst. 34 (2001) 298–310.
[24] P. Hautojärvi in, Positrons in Solids, in: P. Hautojärvi (Ed.), Springer-Verlag, Berlin, 1979, pp. 1–24.
[25] R. Würschum, W. Greiner, R.Z. Valiev, M. Rapp, W. Sigle, O. Schneeweiss, H.E. Schaefer, Interfacial free volumes in ultra-fine grained metals prepared by severe plastic deformation, by spark erosion, or by crystallization of amorphous alloys, Scr. Metal. Mater. 25 (1991) 2451–2456.
[26] J. Čížek, I. Procházka, M. Cieslar, R. Kužel, J. Kuriplach, F. Chmelík, I. Stulíková, F. Bečvář, O. Melikhova, Thermal stability of ultrafine grained copper, Phys. Rev. B 65 (2002) 094106.
[27] L.H. Su, C. Lu, L.Z. He, L.C. Zhang, P. Guagliardo, A.K. Tieu, S.N. Samarin, J.F. Williams, H.J. Li, Study of vacancy-type defects by positron annihilation in ultrafine-grained aluminum severely deformed at room and cryogenic temperatures, Acta Mater. 60 (2012) 4218–4228.
[28] J. Čížek, O. Melikhova, Z. Barnovská, I. Procházka, R.K. Islamgaliev, Vacancy clusters in ultra fine grained metals prepared by severe plastic deformation, J. Phys. Conf. Ser. 443 (2013) 012008.
[29] R.N. West, Positrons in solids, in: P. Hautojärvi (Ed.), Springer-Verlag, Berlin, 1979, pp. 89–144.
[30] U.F. Kocks, T. Hasegawa, R.O. Scattergood, On the origin of cell walls and of

lattice misorientations during deformation, Scr. Metall. 14 (1980) 449–454.
[31] X.W. Li, Z.G. Wang, Y.W. Zhang, S.X. Li, Y. Umakoshi, Dislocation structure in a fatigued Cu–16at%Al alloy single crystal oriented for double slip, Phys. Status Solidi A 191 (2002) R1–R3.
[32] D. Kuhlmann-Wilsdorf, J.H. van der Merwe, Theory of dislocation cell sizes in deformed metals, Mater. Sci. Eng. 55 (1982) 79–83.
[33] B. Bay, N. Hansen, D.A. Hughes, D. Kuhlmann-Wilsdorf, Overview no. 96 evolution of f.c.c. deformation structures in polyslip, Acta Met. Mater. 40 (1992) 205–219.
[34] Q. Liu, D. Juul Jensen, N. Hansen, Effect of grain orientation on deformation structure in cold-rolled polycrystalline aluminium, Acta Mater 46 (1998) 5819–5838.
[35] R.Z. Valiev, A.V. Korznikov, R.R. Mulyukov, Correlation between strength and microstructure of ball-milled Al–Mg alloys determined by X-ray diffraction, Mater. Sci. Eng. A 168 (1993) 141–148.
[36] R.K. Islamgaliev, F. Chmelík, R. Kužel, Thermal stability of submicron grained copper and nickel, Mater. Sci. Eng. A 237 (1997) 43–51.
[37] B. Oberdorfer, R. Wurschum, Positron trapping model for point defects and grain boundaries in polycrystalline materials, Phys. Rev. B 79 (2009) 184103.
[38] A. Dupasquier, R. Romero, A. Somoza, Positron trapping at grain boundaries, Phys. Rev. B 48 (1993) 9235–9245.
[39] J. Čížek, M. Neslušan, M. Čilliková, A. Mičietová, O. Melikhova, Modification of steel surfaces induced by turning: non-destructive characterization using Barkhausen noise and positron annihilation, J. Phys. D. Appl. Phys. 47 (2014) 445301.
[40] F. Bečvář, J. Čížek, I. Procházka, J. Janotová, The asset of ultra-fast digitizers for positron-lifetime spectroscopy, Nucl. Instrum. Methods A 539 (2005) 372–385.
[41] I. Procházka, I. Novotný, F. Bečvář, Application of maximum-likelihood method to decomposition of positron-lifetime spectra to finite number of components, Mater. Sci. Forum 255–257 (1997) 772–774.
[42] M.J. Puska, R.M. Nieminen, Theory of positrons in solids and on solid surfaces, Rev. Mod. Phys. 66 (1994) 841–897.
[43] M.J. Puska, R.M. Nieminen, Defect spectroscopy with positrons: a general calculational method, J. Phys. F. 13 (1983) 333–346.
[44] E. Boroński, R.M. Nieminen, Electron-positron density-functional theory, Phys. Rev. B 34 (1986) 3820–3831.
[45] T. Ungár, I. Dragomir, A. Révész, A. Borbély, The contrast factors of dislocations in cubic crystals: the dislocation model of strain anisotropy in practice, J. Appl. Cryst. 32 (1999) 992–1002.
[46] Y.K. Park, J.T. Waber, M. Meshii, C.L. Snead, C.G. Park, Dislocation studies on deformed single crystals of high-purity iron using positron annihilation: determination of dislocation densities, Phys. Rev. B 34 (1986) 823–836.
[47] C. Hidalgo, G. Donzáles-Doncel, S. Linderoth, J.S. Juan, Structure of dislocations in Al and Fe as studied by positron-annihilation spectroscopy, Phys. Rev. B 45 (1992) 7017–7021.
[48] J. Čížek, I. Procházka, J. Kočík, E. Keilová, Positron lifetime study of reactor pressure vessel steels, Phys. Status Solidi A 178 (2000) 651–662.
[49] Y.Z. Chen, G. Csiszár, J. Čížek, C. Borchers, T. Ungár, S. Goto, R. Kirchheim, On the formation of vacancies in α-ferrite of a heavily cold-drawn pearlitic steel wire, Scr. Mater 64 (2011) 390–393.
[50] L.C. Smedskjaer, M. Manninen, M.J. Fluss, An alternative interpretation of positron annihilation in dislocations, J. Phys. F. Met. Phys. 10 (1980) 2237–2249.
[51] H. Häkkinen, S. Mäkinen, M. Manninen, Positron states in dislocations: shallow and deep traps, Europhys. Lett. 9 (1989) 809–814.
[52] Y. Kamimura, T. Tsutsumi, E. Kuramoto, Calculations of positron lifetimes in a jog and vacancies on an edge-dislocation line in Fe, Phys. Rev. B 52 (1995) 879–885.
[53] A. Vehanen, P. Hautojärvi, J. Johansson, J. Yli-Kauppila, P. Moser, Vacancies and carbon impurities in α- iron: electron irradiation, Phys. Rev. B 25 (1982) 762–780.
[54] C.C. Fu, F. Willaime, P. Ordejón, Stability and mobility of mono- and di-interstitials in α-Fe, Phys. Rev. Lett. 92 (2004) 175503.
[55] P.H.R. Pereira, R.B. Figueiredo, P.R. Cetlin, T.G. Langdon, An examination of the elastic distortions of anvils in high-pressure torsion, Mater. Sci. Eng. A 631 (2015) 201–208.
[56] A.H.W. Ngan, M. Wen, Atomistic simulation of energetics of motion of screw dislocations in bcc Fe at finite temperatures, Comp. Mater. Sci. 23 (2002) 139–145.
[57] D. Cailard, Kinetics of dislocations in pure Fe. Part I. In situ straining experiments at room temperature, Acta Mater. 58 (2010) 3493–3503.
[58] R.Z. Valiev, YuV. Ivanisenko, E.F. Rauch, B. Baudelet, Structure and deformation behaviour of Armco iron subjected to severe plastic deformation, Acta Mater 44 (1996) 4705–4712.
[59] M.J. Zehetbauer, H.P. Stüwe, A. Vorhauer, E. Schafler, J. Kohout, The role of hydrostatic pressure in severe plastic deformation, Adv. Eng. Mater. 5 (2003) 330–337.
[60] E. Schafler, Effects of releasing the hydrostatic pressure on the nanostructure after severe plastic deformation of Cu, Scr. Mater 62 (2010) 423–426.
[61] M.J. Zehetbauer, J. Kohout, E. Schafler, F. Sachslehner, A. Dubravina, Plastic deformation of nickel under high hydrostatic pressure, J. Alloys Comp. 378 (2004) 329–334.
[62] P.A. Varotsos, K.D. Alexopoulos, Thermodynamics of Point Defects and Their Relation with Bulk Properties, North Holland, Amsterdam, 1986.
[63] S. Mukherjee, R.E. Cohen, O. Gülseren, Vacancy formation enthalpy at high pressures in Tantalum, J. Phys. Condens. Matter. 15 (2003) 855–861.
[64] S.M. Kim, W.J.L. Buyers, Vacancy formation energy in iron by positron annihilation, J. Phys. F. Metal. Phys. 8 (1978) L103–L108.
[65] C. Borchers, C. Garve, M. Tiegel, M. Deutges, A. Herz, K. Edalati, R. Pippan, Z. Horita, R. Kirchheim, Nanocrystalline steel obtained by mechanical alloying of iron and graphite subsequently compacted by high-pressure torion, Acta Mater. 97 (2015) 207–215.
[66] H. Halfa, Recent trends in producing ultrafine grained steels, J. Miner. Mater. Charact. Eng. 2 (2014) 428–469.
[67] G.I. Taylor, The mechanism of plastic deformation of crystals. Part I. Theoretical, Proc. R. Soc. Lond. A 145 (1934) 362–387.
[68] N.J. Petch, The ductile-brittle transition in the fracture of α-iron: I, J. Phil. Mag. 3 (1958) 1089–1097.
[69] G.I. Taylor, Plastic Strain in Metals, J. Inst. Met. 62 (1938) 307–324.
[70] X.F. Fang, W. Dahl, Strain hardening of steels at large strain deformation. Part I: Relationship between strain hardening and microstructures of b.c.c. steels, Mater. Sci. Eng. A 203 (1995) 14–25.
[71] H.K.D.H. Bhadeshia, Steels for bearings, Prog. Mater. Sci. 57 (2012) 268–435.
[72] A.S. Keh, S. Weissman, Electron Microscopy and Strength of Crystals, John Wiley & Sons, New York, 1962, p. 231.
[73] W. Morrison, The Effect of Grain Size on the Stress-strain Relationship in Low Carbon Steel, Trans. Am. Soc. Metals 59 (1996) 824–846.
[74] J.P. Hirth, J. Lothe, Theory of Dislocations, McGraw-Hill, New York, 1968.